ELSEVIER

Contents lists available at ScienceDirect

Sensors and Actuators A: Physical

journal homepage: www.elsevier.com/locate/sna



A two-axis water-immersible micro scanning mirror using hybrid polymer and elastomer hinges



Xiaoyu Duan^a, Shuangliang Li^a, Anthony Medellin^b, Chao Ma^b, Jun Zou^{a,*}

- ^a Department of Electrical and Computer Engineering, Texas A&M University, College Station, TX, 77843, USA
- b Department of Engineering Technology and Industrial Distribution, Texas A&M University, College Station, TX, 77843, USA

ARTICLE INFO

Article history: Received 6 January 2020 Received in revised form 13 May 2020 Accepted 25 May 2020 Available online 30 May 2020

Keywords: Hybrid hinges Elastomer nanocomposite Water-immersible scanning mirror Photoacoustic and ultrasound microscopy

ABSTRACT

This paper reports a new two-axis water-immersible micro scanning mirror using hybrid polymer and elastomer hinges. The fast- and slow-axis hinges were made of stiff BoPET (biaxially-oriented polyethylene terephthalate) and soft elastomer nanocomposite (EN) loaded with alumina nanoparticles. Different concentrations of alumina nanoparticles in the base elastomer resin were tested to tune the elastic modulus of the elastomer nanocomposite. The testing results have shown a resonance frequency of 226 Hz for the fast axis and no mechanical resonance for the slow axis when the scanning mirror was immersed in water. 2D B-scan and 3D volumetric ultrasound microscopy were demonstrated by using the hybrid-hinge scanning mirror. The ability of scanning the slow axis at DC or very low frequencies allows a dense raster scanning pattern to be formed for improving both the imaging resolution and field of view.

© 2020 Elsevier B.V. All rights reserved.

1. Introduction

Recently, water-immersible micro scanning mirrors have been developed to provide fast scanning of optical and ultrasound beams in water for not only optical but also photoacoustic and ultrasound microscopy [1-3]. In photoacoustic and ultrasound microscopy, a focused laser or ultrasound pulse is incident onto the target, and the laser-generated or back-scattered ultrasound signal is received with a transducer, which provides one scan point or one pixel for image reconstruction. Depending on the power handling capability of the pulsed laser or ultrasound pulser-receiver, the repetition rate of the laser or ultrasound excitation pulses is usually limited to 10 s of kHz or less [4]. In order to provide high pixel density for image reconstruction, the ideal scanning frequencies of the fast and slow axes of the scanning mirror need to be $100\sim500\,\mathrm{Hz}$ and DC $\sim10\,\mathrm{Hz}$, respectively. To achieve the most energy-efficient driving conditions, the driving frequencies of the two scanning axes should be close to their resonance. Therefore, it is desired that the fast and slow axes possess significantly distinct resonance frequencies.

Different from conventional silicon-based scanning mirrors [4–9], torsional hinges made of high-strength polymer materials, such as BoPET (biaxially-oriented polyethylene terephthalate), are oftentimes used in the water-immersible scanning mirrors to avoid possible damage due to turbulence or shock in water [10–14]. For

BoPET, with a Young's modulus of several GPa, a short torsion hinge is needed to provide desirable stiffness to maintain a stable scanning motion. Such kind of hinge design typically results in a resonance frequency of $100 \sim 500\,\mathrm{Hz}$, which is ideal for the fast axis. However, to achieve a resonance frequency of several Hz or less for the slow axis, long and slender torsion hinges have to be used. However, their bending stiffness will be too low for maintaining a stable scanning motion. Previously, torsion hinges made of PDMS (polydimethylsiloxane) were used in a two-axis water-proof scanning mirror to provide a resonance frequency of 50 and 30 Hz for the fast and slow axes, respectively [3]. However, due to the soft nature of PDMS, it is difficult to further increase the fast-axis resonance frequency and decrease that of the slow axis. Therefore, with a single hinge material, it is quite challenging to obtain two drastically different resonance frequencies by changing the geometries or dimensions of the hinges.

In this paper, we report a new hybrid hinge structure for two-axis water-immersible micro scanning mirrors, which consists of a BoPET hinge for the fast axis and a new elastomer nanocomposite (EN) hinge for the slow axis. Compared with BoPET, the elastomer nanocomposite has a much lower Young's modulus (e.g., several MPa), which can be tuned by changing the mixing ratio of nanoparticles in the elastomer resin. With the proper hinge designs, both suitable torsional and bending stiffness and ultra-low resonance frequencies can be obtained. In addition, the high elastic strain of the elastomer nanocomposite makes it possible to enlarge the tilting angles without degrading or damaging the torsion hinges. For demonstration, a prototype two-axis water-immersible micro

^{*} Corresponding author. E-mail address: duanxiaoyu@tamu.edu (X. Duan).

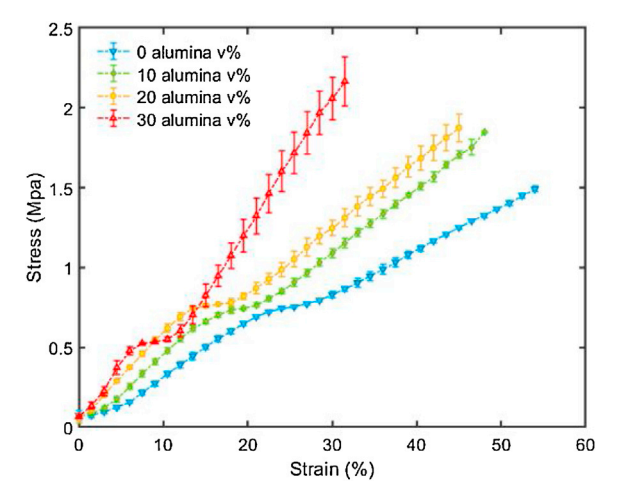


Fig. 1. The stress vs. strain for the tested EN samples with different concentrations of alumina nanoparticles.

scanning mirror using hybrid BoPET/EN hinges has been designed, fabricated and tested. Using the new scanning mirror, scanning ultrasound microscopy has also been conducted with improved spatial resolution and field of view.

2. Preparation and characterization of elastomer nanocomposite

The elastomer nanocomposite was made of a photosensitive base resin loaded with hard nanoparticles as the reinforcement material. The base resin (Flexible Resin, XYZprinting Inc.) was composed of acrylate monomer, polyurethane acrylate, and diphenyl(2,4,6-trimethybenzoyl) phosphine oxide. The viscosity of the resin was 560 cP before the reinforcement material was added. Spherical alumina (Al₂O₃) nanoparticles with an average diameter of 800 nm (US Research Nanomaterials) were used as the reinforcement material. The composite was prepared by magnetically mixing the alumina nanoparticles in the based resin at 200 RPM for 30 min in a dark environment to avoid unwanted photopolymerization. Different concentrations of alumina nanoparticles ranging from 10 % to 30 % were tested. As more alumina nanoparticles were added into the base resin, the aggregation of alumina nanoparticles became more severe and the viscosity of the suspension increased dramatically, making the mixing more difficult and the distribution of the alumina nanoparticles in the base resin less uniform. Therefore, in this work, the highest concentration of alumina nanoparticles was limited to 30%.

After the suspension was fully mixed, it was placed in the resin tank of an optical 3D printer (Nobel Superfine, Xyzprinting Inc.) for photo-polymerization. The addition of a high concentration of alumina particles can cause unwanted optical absorption and scattering. To ensure uniform light dosage through the entire thickness of the EN sample, the optical exposure was performed on a thin layer (25- μ m thick) at a time and repeated until the desirable thickness (1 mm) was reached. A polydimethylsiloxane (PDMS) layer was added to the bottom of the resin tank to assist in the removal of the exposed EN sample was rinsed in ethyl alcohol, dried in air for 5 min, and thermally cured at 60 $^{\circ}$ C for 2 h.

To characterize the mechanical properties of the EN sample, a tensile testing was performed on a Tinius Olsen H10KT Universal Testing Machine using ASTM Standard D1708–18. The EN sample was laser cut into the required shapes and sizes for the tensile testing. The speed of testing was set to 10 mm/min. Fig. 1 shows the measured stress vs. strain for the EN samples with different

Table 1Testing results of different EN samples.

Volume percent of alumina in base resin	0%	10 %	20 %	30 %
Young's modulus (MPa)	3.18	4.85	5.26	7.69
Tensile strength (MPa)	1.49	1.81	1.84	2.11
Elongation (%)	56.39	48.03	45.55	32.70

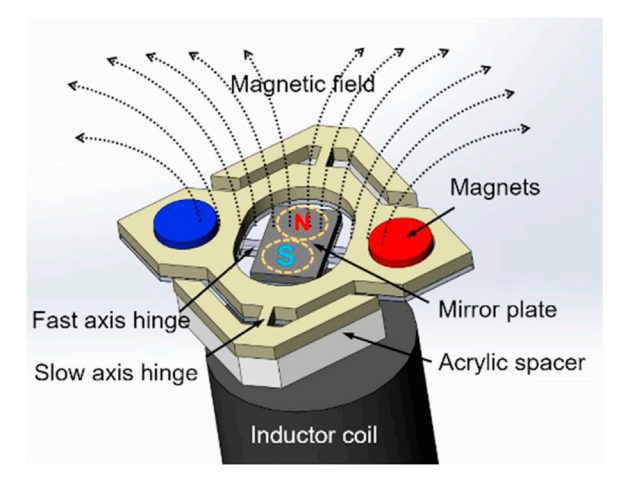


Fig. 2. Schematic design of the two-axis water-immersible scanning mirror with hybrid BoPET and EN hinges.

concentrations of alumina nanoparticles. For each concentration, three samples were tested, from which the average and standard deviation of the stress for certain strain were calculated. The stress increases almost linearly with the strain before the fracture occurs, which indicates the deformation is mostly elastic. The Young's modulus (calculated from the slope of the stress-strain curve), tensile strength, and maximal elongation of the tested samples are listed in Table 1. As expected, both the Young's modulus and tensile strength increases when a higher concentration of alumina particles is loaded into the base resin. The maximal elongation drops as a larger portion of the material becomes rigid. Nevertheless, the maximal elongation of the composite is still much larger than that of other commonly used hinge materials, such as silicon and BoPET.

3. Mirror design and fabrication

3.1. Mirror design

Fig. 2 illustrates the schematic design of the two-axis waterimmersible scanning mirror with hybrid BoPET and EN hinges. It consists of one reflective mirror plate, two hinge layers (BoPET and EN), one support frame and holder, one inductor coil, and two pairs of permanent magnets. The mirror plate is fixed onto the BOPET hinge layer (for the fast axis), which is bonded with the EN hinge layer (for the slow axis). The mirror plate and the two hinge layers are mounted onto the inductor coil via the support frame. One pair of permanent magnets with opposite magnetization are attached onto the bottom surface the mirror plate and the top surface of the EN hinge layer, respectively. To drive the two scanning axes, two AC currents ($I_f sin 2\pi f_f t$ and $I_s sin 2\pi f_s t$) are passed through the coil, which generate two alternating magnetic field to interact with the two pairs of permanent magnets to tilt the mirror plate around the BoPET and EN hinges, respectively. To achieve most energyefficient driving conditions, the frequencies of the two AC currents should match the resonance frequencies (f_{f-s} and f_{r-s}) of the two axes, which can be treated as two (mechanical) bandpass filters. Because the resonance frequencies of the fast and slow axes are drastically different (e.g., 100 s of Hz vs. several Hz), the tilting

Table 2 Main design parameters of the scanning mirror.

	Fast axis	Slow axis
Rotational mirror plate dimension	5 mm × 3 mm	17 mm × 10 mm
Hinge length (L)	0.5mm	2mm
Hinge width (w)	1.5mm	0.5mm
Permanent magnet distance	3mm	10mm
Young's modulus (E)	2.95 GPa [15]	7.69Mpa
Shear modulus (G)	1.53Gpa	2.91Mpa
Poisson ratio [15]	0.38	0.38
Fixed Inductor		
Inductance	10 mH	
Diameter	11.5mm	
Length	15mm	
Permanent magnet		
Diameter	3.1mm	
Height	1.6mm	
Density	$7.5 g/cm^3$	
Environmental Viscosity [16]		
Air	18.6 μPa-s	
Water	1.002 mPa-s	

motion of the fast and slow axes will be decoupled through the dynamic structural filtering effect, and therefore can be independently controlled with the amplitude of the two AC driving currents (I_f and I_s), respectively [12].

Based on the main design parameters of the scanning mirror (Table 2), the torsional resonance frequencies of the two axes in air $(f_{r \ air})$ are estimated by

$$f_{r_air} = \frac{1}{2\pi} \sqrt{\frac{GK}{JL}} \tag{1}$$

Where G is the shear modulus, K is the torsional force constant of the hinge, J is the torsional moment of inertia, and L is the length of hinge. To determine the torsional moment of inertia, the silicon mirror plate and the outer frames are treated as distributive mass, while the permanent magnets are considered as point mass. Thus, the torsional moment of inertia of the fast and slow axis are calculated as

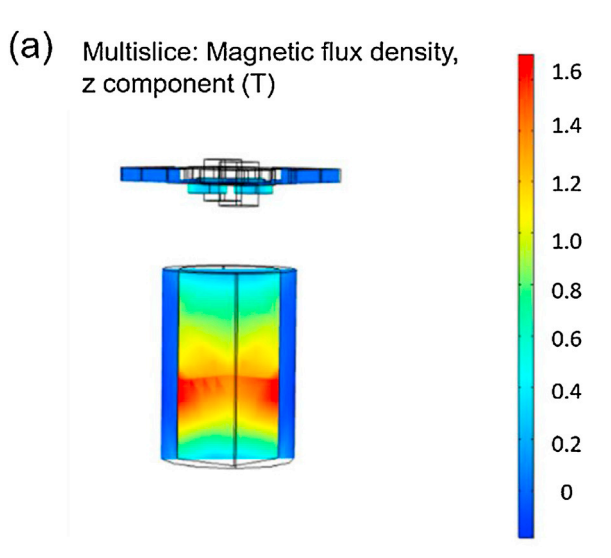
$$J = J_{beam} + nM_{magnet}r^2 \tag{2}$$

Where n is the number of permanent magnets along the fast or slow axis, $M_{\rm magnet}$ is the mass of a single magnet and r is the distance from the center of magnet to the rotating axis. The resonance frequency (f_{r_water}) when the scanning mirror is immersed in water was estimated by

$$f_{r_water} = f_{r_{air}} \sqrt{1 + \frac{3\pi\rho b}{2\rho_m t'}}^{-1} \Gamma_t(k)$$
(3)

Where ρ is the density of water, ρ_m and b are the effective density and width of the scanning mass, $\Gamma_t(k)$ is hydrodynamic functions, and k is normalized mode number [13]. Based on Eqs. (1) and (2), the estimated resonance frequencies of fast axis and slow axis are 309.17 Hz and 4.49 Hz in air, and 231.02 Hz and 3.21 Hz in water, respectively.

To better estimate the scanning performance of the hybrid hinge scanning mirror, finite-element simulation was conducted in COM-SOL Multiphysics®. The AC/DC module was used to calculate the magnetic fields from the inductor coil and permanent magnets and the resulting magnetic forces. The coil was set to be homogenized and circular with an estimated number of turns of 5000. The magnetic flux from the coil was calculated from the driving current. Permanent magnets were simulated by the Ampere's Law. After selecting the domain, the magnetic field was defined by remnant flux density, $B_{\rm r}=0.3\,{\rm Tesla}$. Combining the magnetic fields generated by inductor coil and magnetic fields introduced by permanent magnets (Fig. 3), the magnetic forces applied onto the mirror plate



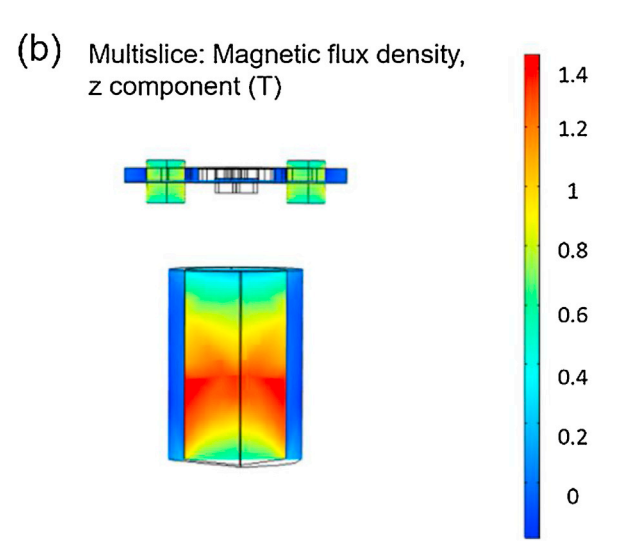


Fig. 3. Simulated magnetic flux density distribution of the fixed inductor and permanent magnets for driving the (a) fast and (b) slow axis.

Table 3Simulated eigen-frequencies of fast and slow axes.

	Fast axis	Slow axis
Eigenfrequency in air (Hz)	280	2.32
Eigenfrequency in water (Hz)	254	2.04

were determined. Next, with the Structural Mechanics module, the magnetic forces were applied to calculate the tilting angles of the mirror plate (Fig. 4). The resonance frequencies of the fast and slow axis were estimated by calculating the eigen-frequencies of the mirror plate structure around the two axes (Table 3), which are slightly lower that those calculated by Eqs. (1) and (3). The scanning angles of the fast and slow axes driven at their resonance frequencies were also simulated. The simulation results are plot together with the measured ones in Fig. 7.

3.2. Mirror fabrication and assembly

Fig. 5 shows the fabrication and assembly process of the hybrid-hinge scanning mirror. Firstly, a 200- μ m-thick aluminum-coated silicon wafer was diced into 5 mm \times 3 mm rectangular pieces to serve as the mirror plate. The two hinge layers for the fast and slow axes were cut out with a CO₂ laser cutter from a 130- μ m thick

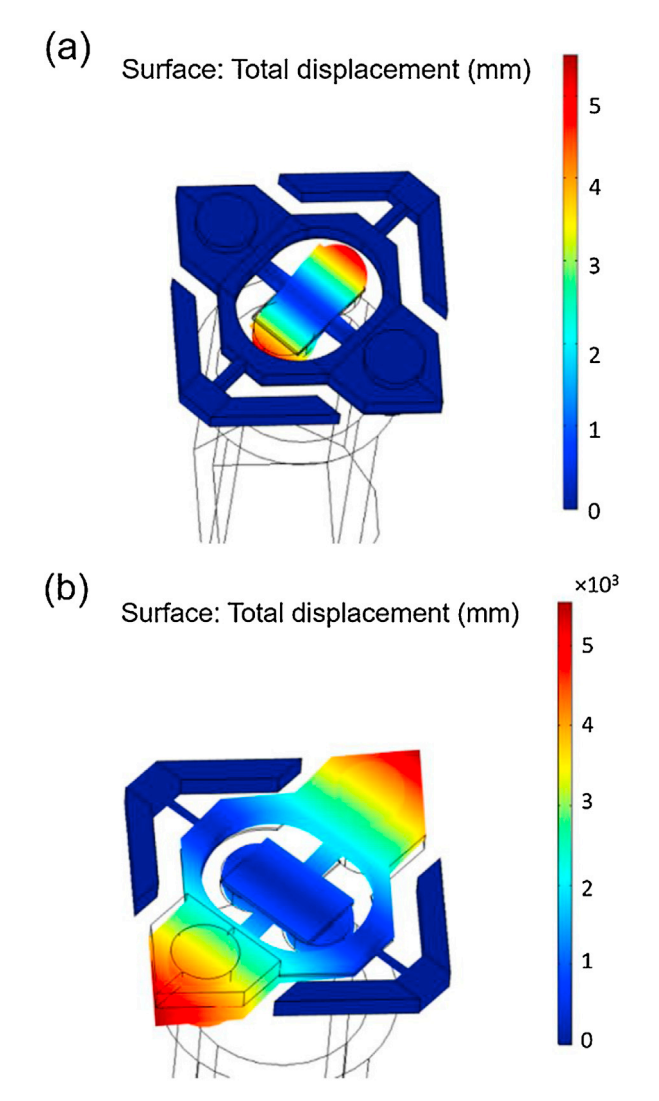


Fig. 4. Simulated vertical displacement of mirror plate around the (a) fast and (b) slow axis

BOPET film and a 1-mm-thick EN sheet, respectively. Two alignment holes were also formed in the EN hinge layer to facilitate the assembly of permeant magnets (Fig. 5(a)). Secondly, the silicon mirror plate and the two hinge layers were bonded together using waterproof silicone glue (Momentive Performance Materials RTV108). One pair of permanent magnet discs (with opposite magnetization polarities) were bonded onto the bottom of the silicon mirror plate. The second pair of permanent magnet discs (with opposite magnetization polarities) were placed in the alignment holes in the EN hinge layer and fixed with the silicone glue (Fig. 5(b)). To increase the magnetic driving force on the slow axis, another pair of permanent magnet discs was attached onto the second pair beneath the BOPET hinge layer. Next, the assembled mirror plate and hinge structure was bonded onto a spacer, which was laser cut from a 2-mm-thick acrylic plate (Fig. 5(c)). Lastly, the entire top structure was mounted onto a 3D-printed plastic holder. The driving inductor coil was inserted inside the holder from the bottom (Fig. 5(d)). Fig. 5(e) and (f) show the top and side views of a fabricated prototype of the hybrid-hinge scanning mirror.

4. Scanning characterization

The characterization of the hybrid-hinge scanning mirror was performed using a laser-tracing method. The scanning mirror was fixed onto a mounting stand at an angle of 45° from a reading screen.

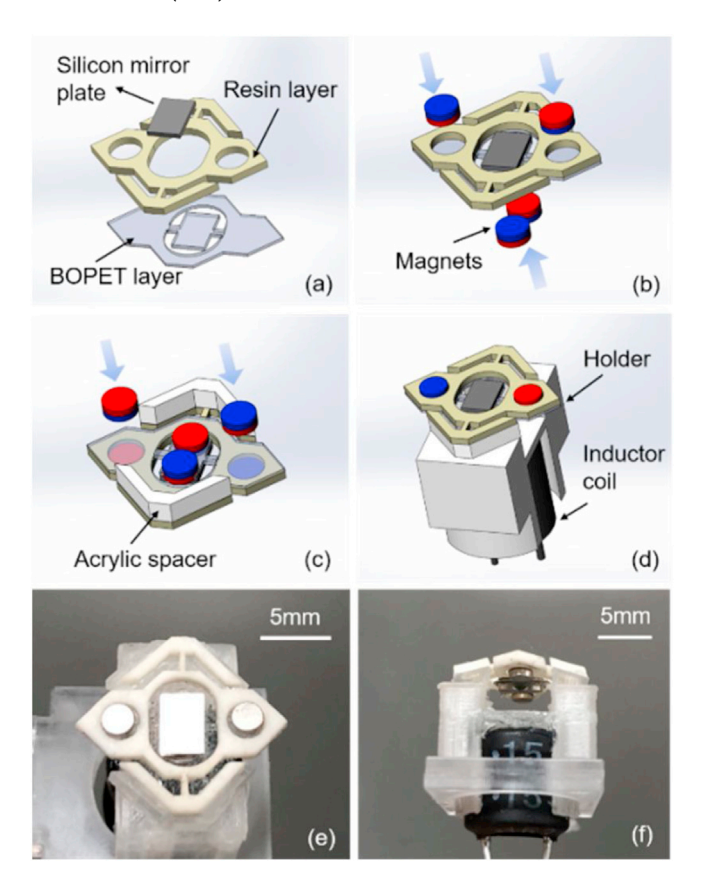


Fig. 5. Fabrication and assembly of two-axis water-immersible scanning mirror with hybrid BoPET and EN hinges: (a)-(d) Fabrication process flow; (d)-(e) Top and side view of a fabricated prototype.

A continuous wave (CW) laser beam was shot onto the center of the mirror plate. The tilting angle of the mirror plate was calculated from the deviation of the laser trace reflected on the reading screen. The resonance frequencies of the fast axis in both air and water were first characterized with an AC driving current of 40 mA in air and 85 mA in water, respectively. The frequency of the AC driving current was varied from DC up to 400 Hz. The resonance frequency is defined as the driving frequency when the tilting angle reaches its maximum. As shown in Fig. 6(a), the resonance frequency of the fast axis is determined to be 295 Hz in air and 226 Hz in water. The quality factor of the fast axis is determined to be 16.5 in air and 9.9 in water, respectively. To characterize the slow axis scanning, the driving frequency was swept from 0 to 40 Hz with 65 mA current in both air and in water. As shown in Fig. 6(b), the tilting angle reaches its maximum at DC, which reveals no meaningful mechanical resonance for the slow axis. This can be explained by the low force constant of the EN torsion hinges and relatively large moment of inertia around the slow axis.

The scanning angles of the fast axis with AC driving and the slow axis with DC driving were characterized and compared with the simulation results. Fig. 7(a) shows both the simulated and measured scanning angles of the fast axis when it is driven at its resonance frequency. When they are small (e.g., $\leq 7^{\circ}$ in air and $\leq 4^{\circ}$ in water), the two scanning angles increase almost linearly with the AC driving current, and the simulation and testing results match well with each other. Beyond certain values, the measured scanning angle will increase more slowly than the simulated one. The deviation becomes more obvious in water and at larger scanning angles. This result shows that the damping on the fast axis is higher in water and also increases with the scanning angle. This can be explained that the liquid damping became stronger as the

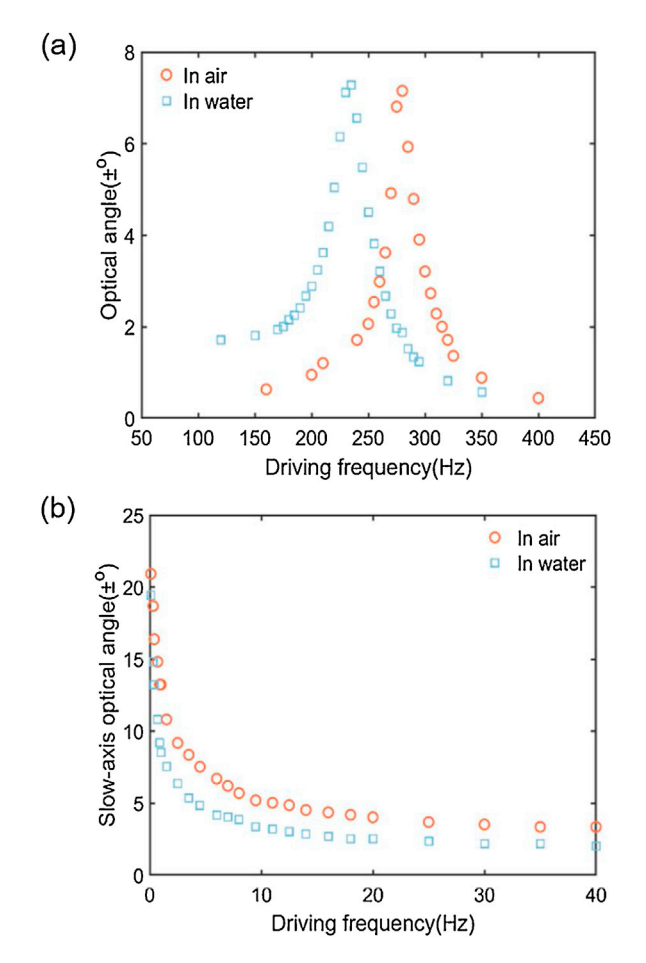


Fig. 6. Optical scanning angle vs. driving frequency of (a) fast axis and (b) slow axis.

vibration of mirror plate getting more intense. Fig. 7(b) shows the simulated and measured scanning angles of the slow axis when it is driven with a DC current. Within the entire scanning range, the scanning angle of the slow axis increase almost linearly with the driving current, and the simulation and testing results match well with each other. This shows that when driven in a quasi-static state at DC, the damping on the slow axis remains almost the same in both air and water and is not significantly affected by the scanning angle.

Raster scanning in water with both axes actuated was tested. The frequency and amplitude of the fast axis driving current was set to be 250 Hz and 55 mA. The slow axis was driven by a DC current increasing from -70 mA to 70 mA with an increment of 2.5 mA for each step. The scanning angle of the fast and slow axes reach $\pm 11^{\circ}$ and $\pm 18^{\circ}$ respectively, which generates a scanning area of $13.6 \, \text{mm} \times 22.7 \, \text{mm}$ at a distance of 35 mm. Fig. 8 shows three representative laser scanning traces when the DC driving current of the slow axis was set to be -50 mA, 0 mA and 50 mA, respectively. The three laser scan traces remain sharp single lines without any broadening, which indicates that the cross-talk between the fast and slow axes is well suppressed. The laser scanning trace of fast axis is slightly distorted when slow axis tilts at larger angles. This is due to the variation of the fast-axis magnets orientation when slow axis is actuated, which results in a small imbalance in the electromagnetic force between two fast-axis magnets. The distortion becomes more severe as the tilting angle increases. Nonetheless, the raster scanning pattern is stable and repeatable. Therefore, this distortion can be calibrated and compensated during image reconstruction. To test its reliability, the fast and slow axes were continuously driven at 226 Hz and 1 Hz, respectively for ~30 h. No significant changes in

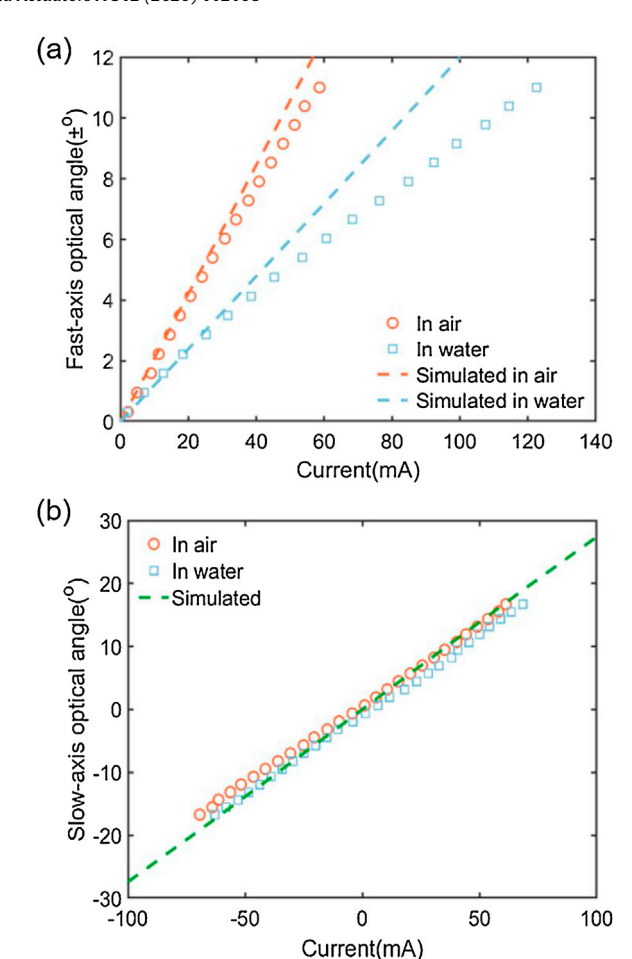


Fig. 7. Optical scanning angle vs. driving current amplitude for (a) fast axis with AC current driving at its resonance frequency and (b) slow axis with DC current driving.

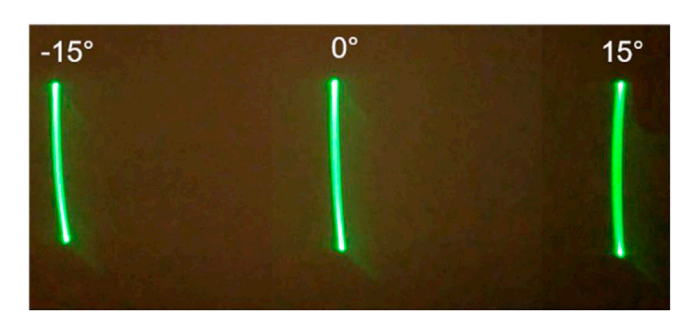


Fig. 8. Representative laser scanning pattern produced by the hybrid hinge mirror with continuous fast-axis scanning and slow-axis tilted at -15°, 0° and 15°.

the scanning performance (e.g., the scanning angle of the two axes and the resonance frequency of the fast axis) were observed.

5. Ultrasound imaging

To demonstrate the unique scanning capability of the hybrid-hinge scanning mirror, a pulse-echo ultrasound microscopic imaging experiment was performed (Fig. 9). The hybrid-hinge scanning mirror, an ultrasound transducer (Olympus V324-SM-F2.00IN-PTF), and an imaging target were immersed in water. The mirror was facing downward at an angle of 45° above the target at a distance of 15 mm. The transducer, with a 25-MHz center frequency and a 50-mm focal length, was placed horizontally toward the mirror at a distance of 35 mm. The target consists of two

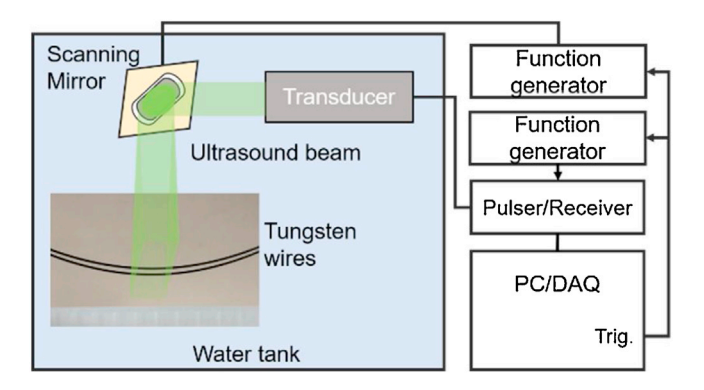


Fig. 9. Schematic of the pulse-echo ultrasound microscopic imaging setup.

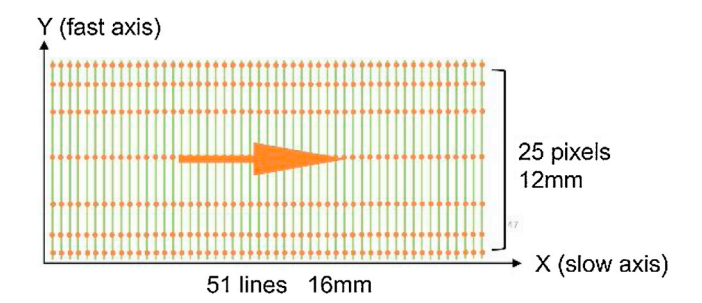


Fig. 10. Simulated 2D scanning pattern with non-overlapping scan points.

curved tungsten wires with a diameter of 430 µm. The two tungsten wires were arranged on an oblique plane and separated from each other by 5 mm (horizontal) and 1 mm (vertical). A pulser/receiver (Olympus 5073PR) was connected to the transducer for ultrasound signal transception. The pulser/receiver was triggered by a function generator with a frequency of 12.5 kHz. A two-channel function generator was used to drive the hybrid-hinge scanning mirror. The frequency and amplitude of the fast axis driving current were set to be 250 Hz and 55 mA. The slow axis was driven by a DC current increased from -50 mA to 50 mA with an increment of 1 mA for each step. The ultrasound echo signal for image reconstruction was recorded by a PC with an add-on data acquisition (DAQ) card (National Instruments PCI 6251). In order to register the corresponding spatial location of each ultrasound echo signal, the two-channel function generator and the pulser/receiver were synchronized by the trigger signal from the DAQ card.

Fig. 10 shows the simulated scanning paths (green lines) of the focal point of the ultrasound transducer. For the fast axis, with a 12.5 kHz ultrasound pulse repetition rate and a 250 Hz scanning frequency, 50 scan points were distributed in one scan cycle. Because the scan points in the first half of the scan cycle (i.e., forward path) overlapped with those in the second half (i.e., reverse path), only the 25 scan points in the first half of the scan cycle were used for image reconstruction. To form 2D scanning, the slow-axis tilting angle was shifted to move the scan path of the fast axis from -15° to 15° in a series of 51 steps. This results in a total of 1275 (51 by 25) scan points distributed in a field of view of 16 mm \times 12 mm.

The ultrasound data processing and imaging reconstruction process is shown in Fig. 11. The 1275 scan points were arranged together to form a 3D data matrix (Fig. 11(a)). At each scan point, the transducer sent an ultrasound pulse and received the backscattered "A-line" echo signal. It should be noted that the scan points are denser near the edges of the scan path due to lower linear scan speed. Therefore, in order to maintain a uniform pixel density, the "A-line" signals obtained at the corresponding 51 scan points along the x-axis (slow axis) were combined to reconstruct a 2D raw B-mode image. The color of the pixels represents the echo signal

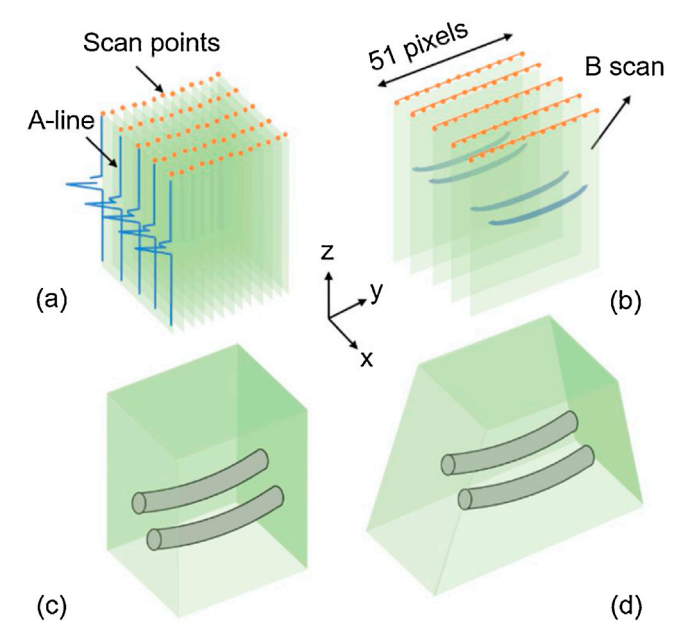


Fig. 11. Illustration of 3D ultrasound image reconstruction process: (a) Regrouping of the scan points; (b) B-scan image reconstruction; (c) SAFT of B-scan images; and (d) Stacking of B-scan images and sector view transformation.

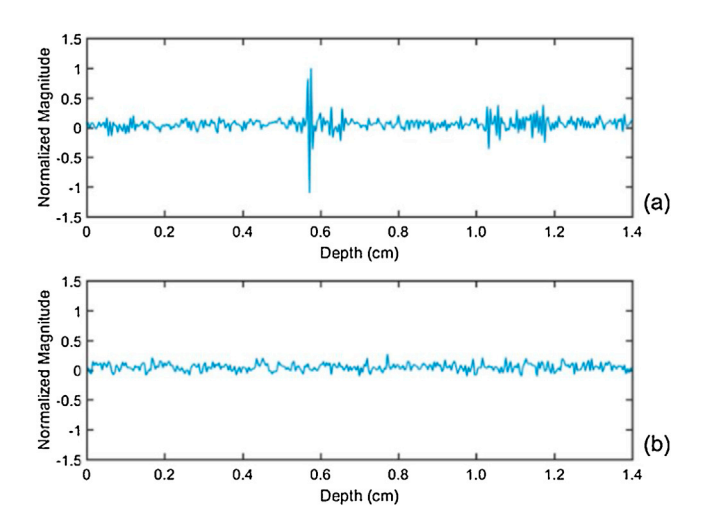


Fig. 12. Representative A-line signals of (a) the target and (b) the background.

intensity. The lateral location of each pixel is determined by the location of the corresponding scan points, while the axial location is determined by its travel time multiplied by sound velocity in water. Next, 2D SAFT (Synthetic Aperture Focusing Technique) [17] was applied on each B-mode image, followed by a sector transformation based on the real dimensions (Fig. 11(b)). This process was repeated until all of the 25 B-mode images were formed. Lastly, all the B-mode images were stacked together to form a 3D volumetric image (Fig. 11(c)), followed by a sector transformation based on the real dimensions (Fig. 11(d)).

Fig. 12(a) and (b) show the typical A-lines echo signals received from the imaging target and the (water) background, respectively. Fig. 13(a) shows one representative raw B-mode image. Because the sound velocity in water (\sim 1540 m/s) is slower than that in tungsten (\sim 5180 m/s), the travel distance per pulse (in other words, axial length per pixel in raw data) in water should be shorter than that in the tungsten targets. An interpolation algorithm based on the ratio between tungsten and water sound velocity was applied on data inside the target to compensate this difference. The B-mode

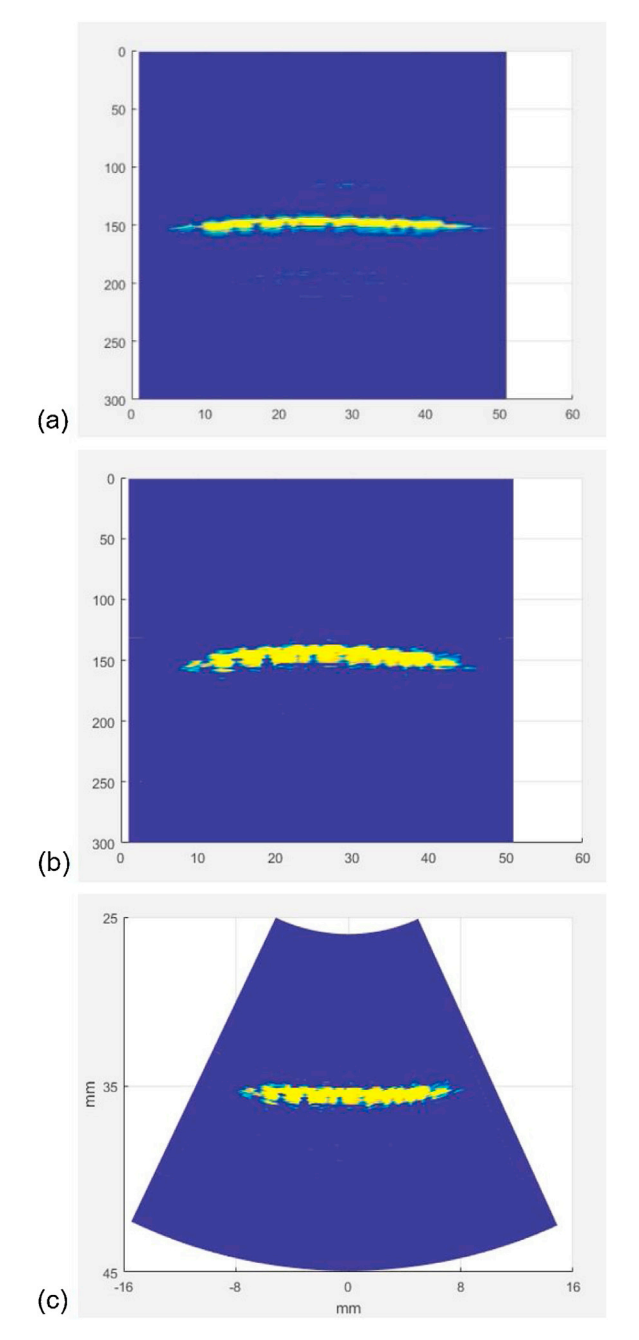


Fig. 13. B-scan image along slow-axis: (a) Before SAFT; (b) After SAFT; and (c) After sector transformation.

image after the application of SAFT and that followed by sector transformation are shown in Fig. 13(c) and (d), respectively. The B-mode images were further stacked to form a 3D volumetric image (Fig. 14) using Volview®. The cuboid transducer field of view is 12 mm in width, 16 mm in length and 20 mm in depth. The lateral resolution is about 1 mm, limited by the transducer focal spot size. It is obvious that the two tungsten wires have distinct curvature, matching with the real target configuration. The lateral and axial intervals between neighboring targets are estimated to be 4 mm and 1 mm, respectively, which are close to the actual distance. In the ultrasound image, the mean diameter of the tungsten wires along the axial direction was estimated to be 450 μ m, which is also close to the actual dimension. It should be noted that at the two ends of the two wire targets, there exist some shrinkage in the diameter. This can be explained by the orientation dependence

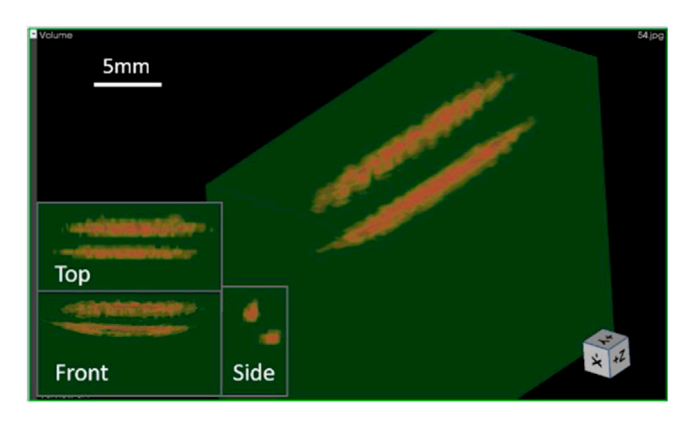


Fig. 14. Reconstructed 3D image of the tungsten wire target.

of ultrasound signal scattering in a relatively large field of view. As the mirror tilting angle increases, a larger portion of the incident ultrasound signals will be scattered away from the transducer, thereby reducing the strength of signals that can be collected by the transducer.

6. Conclusion

In summary, a new elastomer nanocomposite has been investigated as the hinge material for water-immersible micro scanning mirrors. By using BoPET and the elastomer nanocomposite as the fast- and slow-axis hinge materials, a new prototype two-axis water-immersible scanning mirror has been designed, fabricated and tested. The low elastic modulus and high elastic strain of the elastomer nanocomposite make it possible to reduce the resonance frequency of the slow axis down to several Hz or less and increase its maximal tilting angle. Such feature is especially useful for generating a dense raster scanning pattern for scanning optical and acoustic microscopy. For demonstration, scanning ultrasound microscopy has also been conducted with the hybrid-hinge scanning mirror with improvements in both spatial resolution and field of view. Compared with existing MEMS (microelectromechanical systems) scanning mirrors, the overall size of the mirror package is still a little large, which is mainly due to the low patterning resolution of the fabrication process. In the future, a new high-resolution microfabrication process based on photo lithography and etching will be developed to enable further miniaturization of the mirror package.

CRediT authorship contribution statement

Xiaoyu Duan: Methodology, Validation, Data curation, Writing - original draft. **Shuangliang Li:** Software, Validation. **Anthony Medellin:** Investigation, Methodology. **Chao Ma:** Supervision, Conceptualization. **Jun Zou:** Supervision, Conceptualization, Writing - review & editing.

Declaration of Competing Interest

The authors declare that they have no known competing financial interests or personal relationships that could have appeared to influence the work reported in this paper.

Acknowledgments

This work was supported in part by an award (NRI-1748161) from the National Science Foundation and a Prematurity Research Center grant from the March of Dimes Foundation to JZ.

References

- X. Zhang, S.J. Koppal, R. Zhang, L. Zhou, E. Butler, H. Xie, Wide-angle structured light with a scanning MEMS mirror in liquid, Opt. Express 24 (4) (2016) 3479–3487.
- [2] J. Yao, L. Wang, J. Yang, L.S. Gao, K.I. Maslov, L.V. Wang, C.H. Huang, J. Zou, Wide-field fast-scanning photoacoustic microscopy based on a water-immersible MEMS scanning mirror, SPIE J. Biomed. Optics 17 (8) (2012), 080505.
- [3] J.Y. Kim, C. Lee, K. Park, G. Lim, C. Kim, Fast optical-resolution photoacoustic microscopy using a 2-axis water-proofing MEMS scanner, Sci. Rep. 5 (1) (2015) 7932.
- [4] L.V. Wang, S. Hu, Photoacoustic tomography: in vivo imaging from organelles to organs, Science 335 (6075) (2012) 1458.
- [5] K.E. Petersen, Silicon torsional scanning mirror, IBM J. Res. Dev. 24 (5) (1980) 631–637
- [6] D.L. Dickensheets, G.S. Kino, Micromachined scanning confocal optical microscope, Opt. Lett. 21 (10) (1996) 764–766.
- [7] K.H. Gilchrist, D.E. Dausch, S. Grego, Electromechanical performance of piezoelectric scanning mirrors for medical endoscopy, Sens. Actuators A Phys. 178 (5) (2012) 193–201.
- [8] T. Naono, T. Fujii, M. Esashi, S. Tanaka, Non-resonant 2-D piezoelectric MEMS optical scanner actuated by Nb doped PZT thin film, Sens. Actuators A Phys. 233 (2015) 147–157.
- [9] H. Urey, Torsional MEMS Scanner Design for High-Resolution Scanning Display Systems, International Symposium on Optical Science and Technology, SPIE, 2002.
- [10] S. Xu, C.-H. Huang, J. Zou, Microfabricated water-immersible scanning mirror with a small form factor for handheld ultrasound and photoacoustic microscopy, J. Micro/Nanolithography Mems Moems 14 (3) (2015) 1–6, 6.
- [11] S. Xu, J. Zou, Two-axis water-immersible microscanning mirror for scanning optics and acoustic microscopy, J. Micro/Nanolithography Mems Moems 15 (4) (2016) 1–9
- [12] S. Xu, X. Duan, J. Zou, A two-axis water-immersible micro scanning mirror driven by single inductor coil through dynamic structural filtering, Sens. Actuators A Phys. 284 (2018) 172–180.
- [13] C.-H. Huang, J. Yao, L.V. Wang, J. Zou, A water-immersible 2-axis scanning mirror microsystem for ultrasound andha photoacoustic microscopic imaging applications, Microsyst. Technol. 19 (4) (2013) 577–582.
- [14] S. Xu, S. Li, J. Zou, A micromachined water-immersible scanning mirror using BoPET hinges, Sens. Actuators A Phys. 298 (2019), 111564.

- [15] J. Brandrup, E.H. Immergut, E.A. Grulke, Polymer Handbook, 4th ed, John Wiley & Sons, New York, 2005.
- [16] W.M. Haynes, CRC Handbook of Chemistry and Physics, CRC press, 2014.
- [17] C.H. Frazier, W.D.O. Brien, Synthetic aperture imaging with a virtual source element, IEEE Ultrason. Symp. Proc. 2 (1996) 1555–1558.

Biographies

Xiaoyu Duan received her B.S. in microelectronic and optoelectronic engineering from Sun Yat-sen University, P. R. China (2015). She is currently a PhD student in the Department of Electrical Engineering of Texas A&M University. Her major research interests involve underwater optical and acoustic dual modal communication and ranging devices.

Shuangliang Li received his B.S. in microelectronics science and engineering from East China Normal University in 2017. He is currently pursuing the Ph. D in the department of electrical and computer engineering at Texas A&M University. His current research is mainly on MEMS scanning mirrors design and fabrication.

Anthony Medellin received his B.S. in manufacturing and mechanical engineering technology from Texas A&M University, Texas, USA (2020). He is currently pursuing a Ph.D. in the Department of Mechanical Engineering at Texas A&M University. His current research involves nanocomposites in vat photopolymerization.

Chao Ma received his B.E. degree from Tsinghua University in 2010, M.S. degree from University of Wisconsin–Madison in 2012, and Ph.D. degree from University of California, Los Angeles in 2015, all in Mechanical Engineering. Dr. Ma was a senior mechanical engineer at Cymer, LLC., San Diego, CA, from 2015 to 2016. Dr. Ma joined the faculty at Texas A&M University, College Station, TX, in 2016. His research interest is additive manufacturing.

Jun Zou received his Ph.D. degree in electrical engineering from the University of Illinois at Urbana-Champaign in 2002. In 2004, he joined the department of electrical and computer engineering at Texas A&M University, where he is currently a full professor and directs the Micro Imaging and Sensing Devices and Systems (MISDS) Lab. His current research interests lie in the development of micro and nano opto-electro-mechanical devices and systems for biomedical imaging, robotics and artificial intelligence applications. He is a Senior Member of IEEE and SPIE, and a Member of OSA.